Chapter 10
Fabrication, Characterization, and Modulation of Functional Nanolayers

Hiromichi Ohta and Hidenori Hiramatsu

Abstract Regions of a few nanometers at the surface or interface of a material exhibit various functional properties, which differ from those of the bulk because the electrons and/or ions receive different potentials due to the incoherent atomic arrangement. High-quality epitaxial films of functional materials called "nanolayers" are important to utilize such functional properties. However, fabrication of high-quality nanolayers of complex materials with complicated crystal structures is usually challenging due to the difference in the thermochemical properties of the constituents. In this chapter, epitaxial growth techniques, especially "reactive solid-phase epitaxy" of functional oxides and chalcogenides, are reviewed based on the authors' efforts. Additionally, this chapter reviews several modulation methods of optical, electrical, and magnetic properties of functional oxide nanolayers.

Keywords Nanolayers · Epitaxial growth method · Functional oxides and chalcogenides · Modulation methods

H. Ohta (✉)
Research Institute for Electronic Science, Hokkaido University,
N20W10, Kita-ku, 001-0020 Sapporo, Japan
e-mail: hiromichi.ohta@es.hokudai.ac.jp

H. Hiramatsu (✉)
Laboratory for Materials and Structures,
Institute of Innovative Research, Tokyo Institute of Technology,
4259 Nagatsuta-cho, R3-1, 226-8503 Midori-ku, Yokohama, Japan
e-mail: h-hirama@mces.titech.ac.jp

H. Hiramatsu
Materials Research Center for Element Strategy, Tokyo Institute of Technology,
4259 Nagatsuta-cho, SE-6, 226-8503 Midori-ku, Yokohama, Japan

10.1 Epitaxial Growth and Characterization of Functional Nanolayers

Regions of a few nanometers at the surface or interface of a material often exhibit various functional properties, which differ from those of the bulk due to the fact that the electrons and/or ions receive different potentials due to the incoherent atomic arrangement. High-quality epitaxial films of functional materials called "nanolayers" are important to utilize such functional properties.

In this chapter, epitaxial growth techniques, especially "reactive solid-phase epitaxy" of functional oxides and chalcogenides, are reviewed based on the authors' efforts. Additionally, this chapter reviews several modulation methods of optical, electrical, and magnetic properties of functional oxide nanolayers.

10.2 Pulsed Laser Deposition

Pulsed laser deposition (PLD) is a physical vapor deposition technique [1]. By irradiating focused laser pulses of an excimer laser or a higher (3rd or 4th) harmonic of a Nd:YAG laser onto the target material (single crystals or ceramics or powder), which is located in an ultrahigh vacuum chamber, films can be deposited on the substrate as a result of vaporization of the target materials occur during laser irradiation (Fig. 10.1). PLD is one of the most powerful techniques for epitaxial
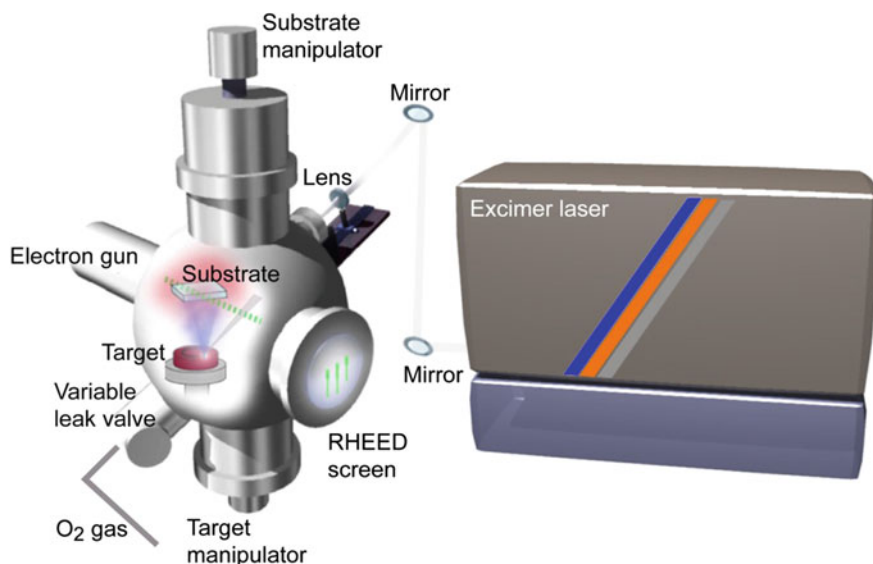

Fig. 10.1 Schematic illustration of a PLD system

film growth of inorganic solids, especially oxides. It has several advantages compared to the other deposition techniques, such as sputtering. In the case of PLD, the chemical composition of the resultant film is almost same as that of the target material, although generally it differs from the target because the chemical species show different sputtering yields in the case of sputtering. Moreover, the atmosphere in the PLD chamber can be widely controlled from an ultrahigh vacuum to $\sim 10^2$ Pa, allowing a thermodynamically nonequilibrium crystalline phase of a material to be fabricated.

As an example, PLD growth and characterization of the $SrTiO_3$-$SrNbO_3$ solid solution system are explained. $SrTiO_3$ has attracted increasing attention as the next generation of *oxide electronics* [2]. Doping with the appropriate substituent, such as Nb^{5+} (Ti^{4+} site) or La^{3+} (Sr^{2+} site), easily varies the charge carrier concentration of $SrTiO_3$ from insulating to metallic ($n_{3D} \sim 10^{21}$ cm^{-3}). Electron-doped $SrTiO_3$ is one of the most extensively studied materials for thermoelectric applications [3, 4]. In 2001, Okuda et al. [5] synthesized $Sr_{1-x}La_xTiO_3$ ($0 \leq x \leq 0.1$) single crystals by the floating-zone method. They reported that the crystals exhibit a large power factor ($S^2 \cdot \sigma$) of 2.8–3.6 mW m^{-1} K^{-2} at room temperature. Later, Ohta et al. reported the carrier transport properties of Nb- and La-doped $SrTiO_3$ single crystals (carrier concentration, $n \sim 10^{20}$ cm^{-3}) at high temperatures (~ 1000 K) to clarify the intrinsic thermoelectric properties of these materials [6].

The experimental discovery of unusually large thermopower outputs from superlattices and two-dimensional electron gases in $SrTiO_3$ [7, 8] spurred substantial research efforts into $SrTiO_3$ superlattices [9, 10] and heterostructures [11–13] for thermoelectric applications. For example, a superlattice composed of one unit cell (uc) of $SrTi_{0.8}Nb_{0.2}O_3$ and 10 uc of $SrTiO_3$ exhibits a giant thermopower, most likely due to an electron confinement effect. Although electron confinement is strongly correlated with the electronic structure [14, 15], a full understanding of the fundamental electronic phase behavior of the $SrTi_{1-x}Nb_xO_3$ solid solution system has yet to be developed.

Although high-quality single crystals of $SrTi_{1-x}Nb_xO_3$ species with $x > 0.1$ are not available due to the low solubility limit of Nb in the lattice [16], epitaxial films with these material compositions can be fabricated by PLD [17]. As summarized in Fig. 10.2, pure $SrTiO_3$ (space group $Pm\bar{3}m$, cubic perovskite structure, $a = 3.905$ Å) is an insulator with a bandgap of 3.2 eV. The bottom of the conduction band is composed of triply degenerate, empty Ti 3d–t_{2g} orbitals, while the top of the valence band is composed of fully occupied O 2p orbitals [18]. The valence state of Ti ions in crystalline $SrTiO_3$ is $4+$ (Ti 3d^0). On the other hand, pure $SrNbO_3$ (space group $Pm\bar{3}m$, cubic perovskite structure, $a = 4.023$ Å) is a metallic conductor [19–21]. The valence state of the Nb ion is $4+$ (Nb 4d^1). In between $SrTiO_3$ and $SrNbO_3$ in the $SrTi_{1-x}Nb_xO_3$ ss, there are two possible types of valence state changes in the Ti and Nb ions, as shown in Fig. 10.2b and c. In the case of isovalent substitution (Fig. 10.2b), the mole fraction of Ti^{4+} proportionally decreases with increasing Nb^{4+} (x). On the other hand, heterovalent substitution, in which two Ti^{4+} or Nb^{4+} ions are substituted by adjacent (Ti^{3+}/Nb^{5+}) ions, can occur, as shown in
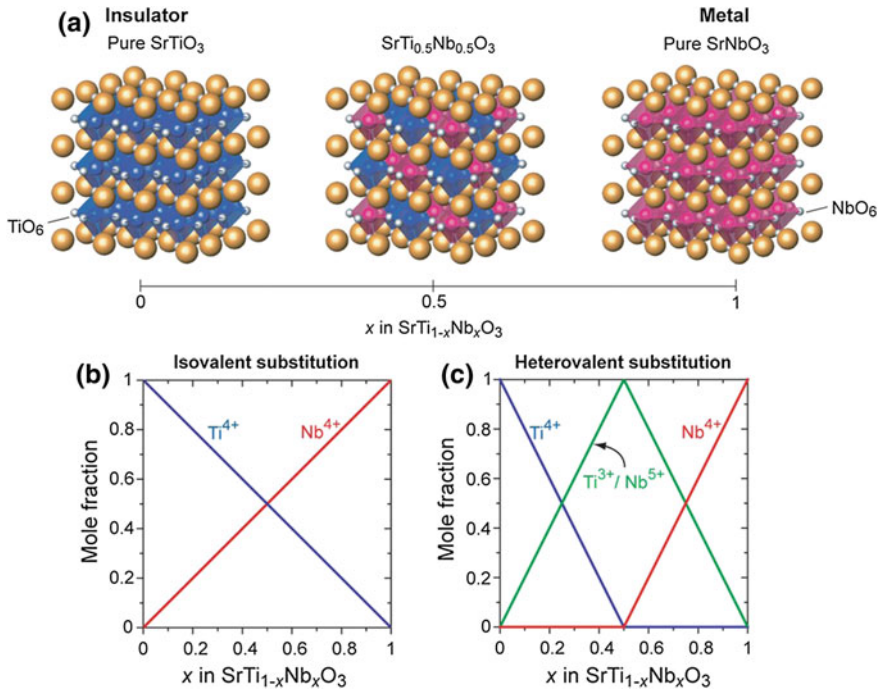
Fig. 10.2 Schematic of the crystal structure and possible valence state changes in the $SrTiO_3$-$SrNbO_3$ solid solution system. **a** Schematic of the crystal structure. Pure $SrTiO_3$ is an insulator with a bandgap of 3.2 eV, in which the valence state of the Ti ions (blue, TiO_6) is 4 + (Ti $3d^0$). In contrast, pure $SrNbO_3$ is a metal, in which the valence state of the Nb ions (Red, NbO_6) is 4 + (Nb $4d^1$). **b, c** Possible valence state changes of the Ti and Nb ions in the $SrTiO_3$-$SrNbO_3$ solid solution system: **b** isovalent substitution, where Ti^{4+} is substituted by Nb^{4+} and **c** heterovalent substitution, where two Ti^{4+}/Nb^{4+} ions are substituted by adjacent Ti^{3+}/Nb^{5+} ions. Reprinted with permission from [22]. © 2017 AIP

Fig. 10.2c. Based on these considerations, we focused on the valence state changes of Ti and Nb ions in the $SrTi_{1-x}Nb_xO_3$ ss.

Zhang et al. [22] fabricated approximately 100 nm-thick $SrTi_{1-x}Nb_xO_3$ ($x = 0.05, 0.1, 0.2, 0.3, 0.4, 0.5, 0.55, 0.6, 0.7, 0.8, 0.9$, and 1.0) epitaxial films by PLD using dense ceramic disks of a $SrTiO_3$-$SrNbO_3$ mixture. Insulating (001) $LaAlO_3$ (pseudo-cubic perovskite, $a = 3.79$ Å) was used as the substrate. The growth conditions were precisely controlled with a substrate temperature of 850 °C, an oxygen pressure of $\sim10^{-4}$ Pa, and a laser fluence of 0.5–1 J cm^{-2} pulse^{-1}, yielding a growth rate of 0.3 pm pulse^{-1}.

Figure 10.3a summarizes the Xray reciprocal space mappings (RSMs) around the ($\bar{1}$03) diffraction spot of $LaAlO_3$ (overlaid). Intense diffraction spots from ($\bar{1}$03) $SrTi_{1-x}Nb_xO_3$ are seen together with those from the $LaAlO_3$ substrate, indicating that incoherent heteroepitaxial growth of the target materials occurs for all x compositions. The peak positions of the diffraction spots from each composition
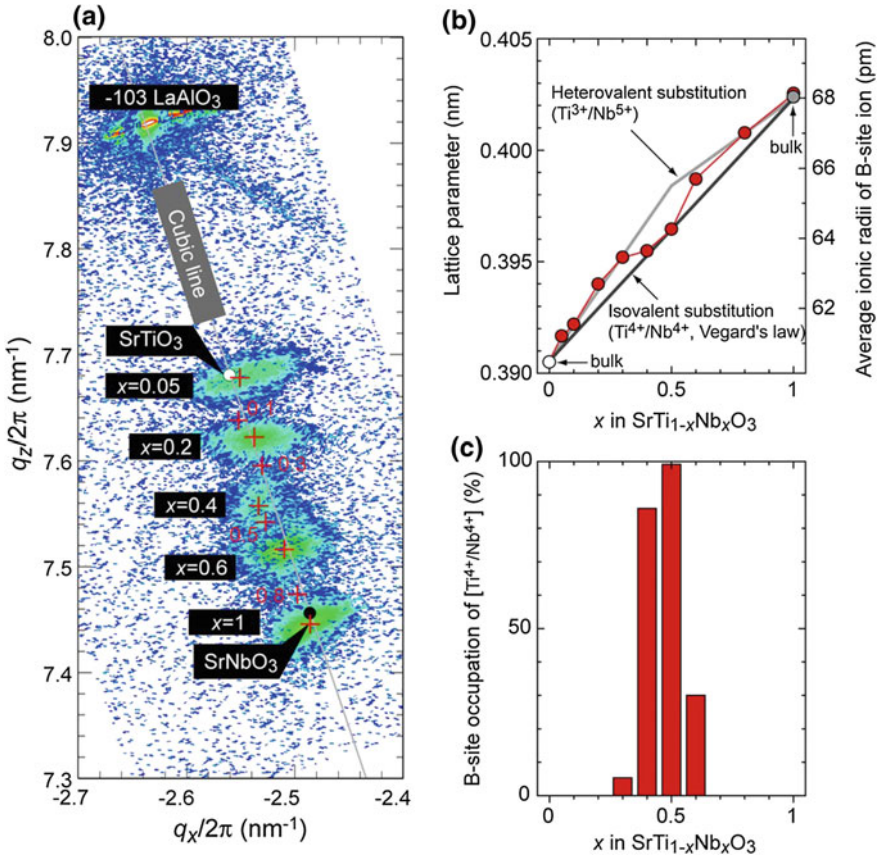
Fig. 10.3 Crystallographic characterization of the $SrTi_{1-x}Nb_xO_3$ epitaxial films on a (001) $LaAlO_3$ single-crystal substrate. **a** Xray reciprocal space mappings around the $(\bar{1}03)$ diffraction spot of the $SrTi_{1-x}Nb_xO_3$ epitaxial films. The location of the $LaAlO_{-3}$ diffraction spot, $(q_x/2\pi, q_z/2\pi) = (-2.64, 7.92)$, corresponds to the pseudo-cubic lattice parameter of $LaAlO_3$ ($a = 0.379$ nm). Red symbols (+) indicate the peak positions of the $SrTi_{1-x}Nb_xO_3$ epitaxial films. **b** Changes in the lattice parameters of the $SrTi_{1-x}Nb_xO_3$ films (circles, left axis) superimposed with isovalent/heterovalent substitution lines (black line: isovalent substitution, gray line: heterovalent substitution, right axis), calculated using Shannon's ionic radii [23]. **c** Changes in the B-site occupation by $[Ti^{4+}/Nb^{4+}]$ derived from the data in (**b**). Reprinted with permission from [22]. © 2017 AIP

correspond well with the cubic line ($q_z/q_x = -3$), suggesting that no epitaxial strain is induced in the films. It should be noted that a slight tetragonal distortion is observed in the $x = 0.4$ ($c/a = 1.0057$) and 0.5 ($c/a = 1.0050$) samples.

From the RSMs of the $SrTi_{1-x}Nb_xO_3$ films, we extracted the lattice parameters using the formula $a = (2\pi/q_x \cdot 2\pi/q_x \cdot 6\pi/q_z)^{1/3}$. Figure 10.3b plots the lattice parameters of the $SrTi_{1-x}Nb_xO_3$ film as a function of x. We observed an M-shaped trend along with a general increase in the lattice parameter with increasing x. In order to analyze the changes in the lattice parameter, we calculated the average
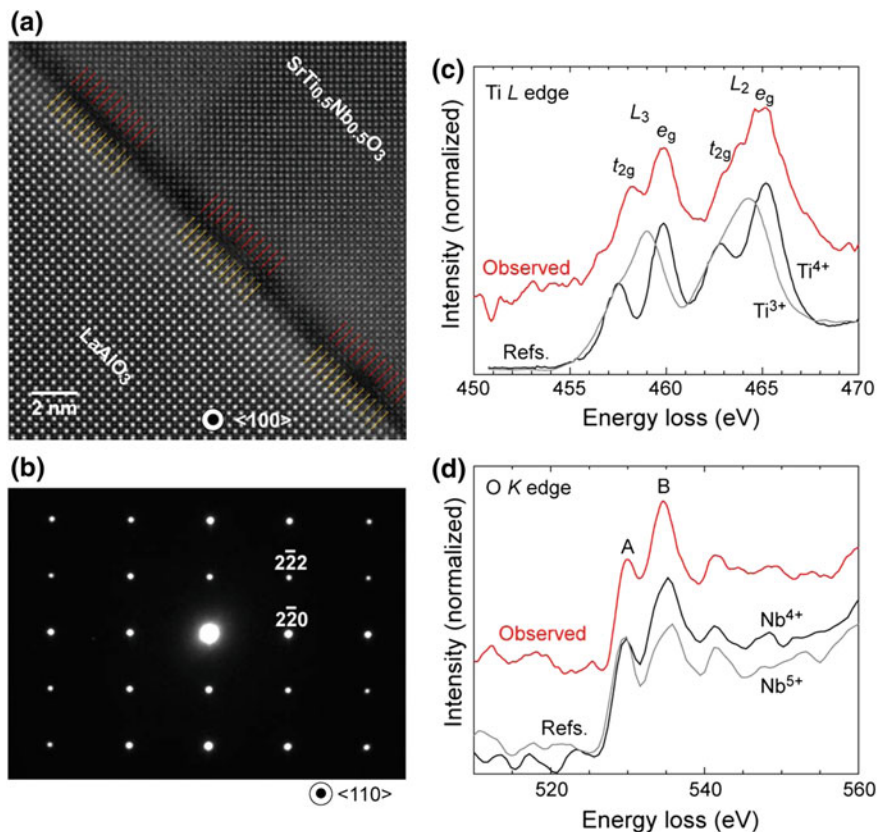
Fig. 10.4 Electron microscopy analyses of a $SrTi_{1-x}Nb_xO_3$ film with a composition of $x = 0.5$. **a** HAADF-STEM image acquired with the electron beam incident along the <100> direction. Periodic misfit dislocations (∼8.5 nm interval) at the heterointerface are indicated by red lines. **b** Selected-area electron diffraction pattern acquired with the electron beam incident along the <110> direction. **c**, **d** EELS spectra acquired around the **c** Ti L edge and **d** O K edge. EELS spectra for Ti^{3+}/Ti^{4+} [27] and Nb^{4+}/Nb^{5+} [28] from previous studies are also plotted for comparison. Reprinted with permission from [22]. © 2017 AIP

ionic radii in the crystal structure and used Shannon's ionic radii as a comparison [23]: Ti^{4+} (60.5 pm), Ti^{3+} (67.0 pm), Nb^{4+} (68.0 pm), and Nb^{5+} (64.0 pm). In the ranges of $0.05 \leq x \leq 0.3$ and $x \geq 0.6$, the observed lattice parameters closely follow the heterovalent substitution line, suggesting that two Ti^{4+} or Nb^{4+} ions are substituted by adjacent (Ti^{3+}/Nb^{5+}) ions [24]. On the other hand, at $x = 0.4$ and 0.5, the observed lattice parameter correspond well with the isovalent substitution line. Moreover, at $x = 0.5$, the B-site occupation of [Ti^{4+}/Nb^{4+}] is almost 100%, as shown in Fig. 10.3c.

Figure 10.4a shows a cross-sectional HAADF-STEM image of the $SrTi_{0.5}Nb_{0.5}O_3$ film. Periodical mismatch dislocations with intervals of ∼8.5 nm are seen at the heterointerfaces. If the strain in the thin film is fully relaxed by such

misfit dislocations, it is possible to calculate the spacing between dislocations (d) from $d = \mathbf{b}/\delta$, where $\mathbf{b}$ is the Burgers vector and δ is the lattice mismatch between thin film and substrate [25]. Using the lattice parameters obtained from XRD [$\delta = (q_{x\,sub} - q_{x\,film})/q_{x\,film} = +0.0435$], the estimated dislocation spacing is 8.7 nm, suggesting that the dislocations fully relax the strain in the film. Although superspots originating from the (111) diffraction are often observed in $AB_{0.5}B'_{0.5}O_3$ compositions that crystallize in B-site-ordered double perovskite structures [26], they are not observed in the $SrTi_{0.5}Nb_{0.5}O_3$ film (Fig. 10.4b). This is most likely due to the slight tetragonal distortion of the crystal structure. Figure 10.4 shows the EELS spectra acquired around the Ti L (c) and O K edges (d). The reported EELS spectra of Ti^{3+}/Ti^{4+} [27] and Nb^{4+}/Nb^{5+} [28] are plotted for comparison. In the Ti L edge spectrum (c), t_{2g} and $e_{.g.}$ peak splitting is clearly observed for Ti L_3, indicating that the dominant valence state of Ti is 4+. In the O K edge spectra (d), two intense peaks (assigned as A and B) are clearly observed where peak B has a higher intensity than peak A. A previous study noted that this is a characteristic feature of Nb^{4+} [28]. The peak intensity ratio A/B is calculated to be 0.66, which roughly corresponds with the Nb^{4+} spectrum (0.66).

By using abovementioned films, Zhang and Ohta et al. clarified the thermoelectric phase diagram for the $SrTi_{1-x}Nb_xO_3$ ($0.05 \le x \le 1$) solid solution system (Fig. 10.5). They observed two thermoelectric phase boundaries in the system, which originate from the step-like decrease in the carrier effective mass at $x \sim 0.3$ and from the local minimum in the carrier relaxation time at $x \sim 0.5$. The origins of these phase boundaries are related to the isovalent/heterovalent B-site substitution. The parabolic Ti 3d orbitals dominate the electron conduction for compositions with $x < 0.3$, whereas the Nb 4d orbital dominates when $x > 0.3$. At $x \sim 0.5$, a tetragonal distortion of the lattice, in which the B-site is composed of Ti^{4+} and Nb^{4+} ions, leads to the formation of tail-like impurity bands, which maximize electron scattering. These results provide a foundation for further research to improve the thermoelectric performance of $SrTi_{1-x}Nb_xO_3$.

Fig. 10.5 Thermoelectric phase diagram for the $SrTiO_3$-$SrNbO_3$ solid solution system. The thermoelectric power factor ($S^2 \cdot \sigma$) of the $SrTiO_3$-$SrNbO_3$ solid solution system is plotted along with the previously reported values [7]. The x dependence of $S^2 \cdot \sigma$ is shown in the inset. The system's thermoelectric phase boundaries are clearly seen at $x \sim 0.3$ and ~ 0.5. Reprinted with permission from [22]. © 2017 AIP
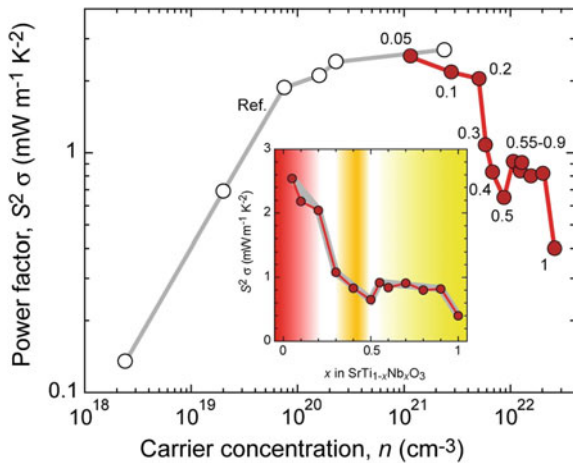
10.3   Reactive Solid-Phase Epitaxy

As explained above, PLD is a powerful technique for epitaxial film growth of metal oxides. Although there are many reports on epitaxial oxide film growth by the PLD method, it is still difficult to fabricate epitaxial films of complex oxides composed of different vapor pressure elements, especially alkali metals. Since complex oxides have high melting points (>1500 °C), substrates must be heated at high temperature (>800 °C : ∼60% of the melting point) in a vacuum during PLD. If the multiplex elements have different vapor pressures at the substrate temperature, the chemical composition of the resultant film completely differs from that of the target because re-vaporization of the high vapor pressure element occurs during deposition.

To overcome this issue, Ohta et al. developed the "Reactive Solid-Phase Epitaxy (R-SPE)" method in 2003 (Fig. 10.6) [29]. In this method, an epitaxial film of a monoxide, which is a component of a complex oxide, is fabricated by PLD. Then the film is heated at high temperatures with another member of the target oxide (thin film or powder). During the heat treatment, a solid-solid reaction between the monoxide film and the other member elements occurs while maintaining the crystallographic orientation. Using the R-SPE method, epitaxial films of InMO$_3$(ZnO)$_m$ (M = Ga and In, m = integer) [29], ZnRh$_2$O$_4$ [30], LaCuOCh (Ch = S or Se) [31], and Na$_x$CoO$_2$ ($x \sim 0.8$) [32] have been fabricated. Thus, the R-SPE method effectively fabricates epitaxial films of complex oxides composed of high vapor pressure elements. In this section, recent progress of "reactive solid-phase epitaxy" of functional oxides and chalcogenides is reviewed.

10.3.1   Na$_{\approx 2/3}$MnO$_2$ Epitaxial Film

Layered alkali ion-containing metal oxides (LAMO), $A_x M$O$_2$ (A: alkali metal and M: transition metal) have received considerable interest as candidate materials for energy storage and conversion applications. This is because their chemical potential can be readily controlled. Changing the concentration of A^+ in the interspace between adjacent MO$_2$ layers tunes the valence state of the M ion. In particular, there have been many studies on cobalt-based A_xCoO$_2$ because the A^+ concentration is easily controlled and these oxides possess a two-dimensional electronic structure. Li$_x$CoO$_2$ ($0 \leq x \leq 1$) is one of the best cathode active materials in commercial Li-ion batteries because the Li$^+$ concentration can be controlled by an electrochemical process [33, 34]. Meanwhile, Na$_x$CoO$_2$ ($x \sim 0.8$) is a promising thermoelectric material, which can directly convert a temperature difference into electricity. Additionally, it exhibits a rather large thermopower even though it displays metallic conductivity due to the two-dimensional nature of the electronic structure [35, 36]. Furthermore, the two-dimensional electronic structure of the bilayer hydrated crystal Na$_{\approx 0.3}$CoO$_2$ · 1.3H$_2$O allows it to exhibit superconductivity at a critical temperature T_c of ∼4 K [37, 38].
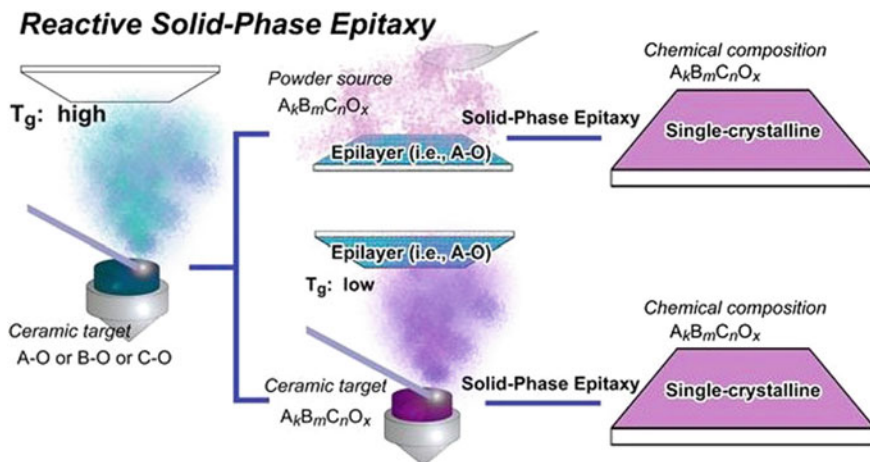
Fig. 10.6 Schematic diagram of the "Reactive Solid-Phase Epitaxy" method. A bilayer laminate composed of a thin epitaxial layer of simple oxide (A–O or B–O or C–O) or metal grown on a substrate and a polycrystalline layer or powder source of target $A_kB_mC_nO_x$ is thermally annealed at high temperatures (~1000 °C). The solid-state reaction at high temperatures leads to the formation of a thin single-crystalline layer on the substrate, which may act as "an epitaxial template" for successive homoepitaxial SPE growth of the film

Unlike A_xCoO_2 systems, the physical properties of A_xMnO_2 have yet to be clarified, although Na_xMnO_2 has recently been proposed as a new candidate for the cathode active material in Na-ion batteries [39–41] because Mn (Clarke number: 0.09) is more abundant than Co (Clarke number: 0.004). At least two crystallographic phases of $NaMnO_2$ are known; low-temperature α-$NaMnO_2$ [39, 42] has an O3 layered structure with monoclinic symmetry and high-temperature β-$NaMnO_2$ [40] has a *Pmnm* structure with orthorhombic symmetry. It should be noted that the crystal symmetry of Na_xMnO_2 strongly depends on x. The low-temperature phase $Na_{0.67}MnO_2$ [41, 43] has a P2 layered structure with hexagonal symmetry. Recently, Billaud et al. [41] reported that $Na_{0.67}MnO_2$ with a P2 structure exhibits a high capacity of 175 mA h g^{-1} with a good capacity retention.

However, there are a few studies on the electrical conductivity of Na_xMnO_2 [44]. The most rational reason is the lack of large single crystals. It is difficult to measure the intrinsic electrical property using powder compacts due to severe electron scattering. High-quality epitaxial films may be a solution to clarify the electrical conductivity of Na_xMnO_2.

In 2017, Katayama et al. fabricated Na_xMnO_2 epitaxial films by the R-SPE method using the following procedure (Fig. 10.7) [45]. First, a 70 nm-thick MnO_y thin film was heteroepitaxially grown on a (0001) α-Al_2O_3 substrate (10 × 10 × 0.5 mm) by PLD using a KrF excimer laser ($\lambda = 248$ nm, 20 ns, 10 Hz, ~1.5 J cm^{-2} $pulse^{-1}$) to ablate the Mn_2O_3 ceramic disk. During the deposition, the substrate temperature and oxygen pressure were kept at 700 °C and ~10^{-2} Pa, respectively. After deposition,
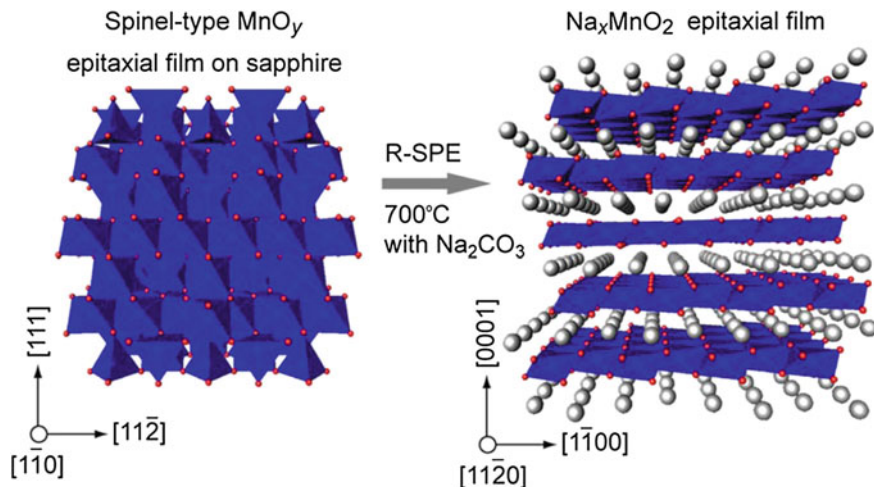
Fig. 10.7 Schematic of the crystal structure change from MnO_y to Na_xMnO_2 during R-SPE [Gray: Na, blue: Mn, red: O]. First, a spinel-type MnO_y film is heteroepitaxially grown on a sapphire substrate. The MnO_y epitaxial film, covered with Na_2CO_3 powder, is heated at 700 °C in air. As a result, Na^+ ions are supplied into the MnO_y film together with O^{2-} ions during the heating, forming the Na_xMnO_2 epitaxial film with a layered crystal structure. Reprinted with permission from [45]. © 2017 ACS

the film was cooled to RT in the PLD chamber. The film's top surface was completely covered with another sapphire plate, and the sandwiched specimen was subsequently preserved in Na_2CO_3 powder. Then the film was heated at 700 °C for 30 min in air to supply Na^+ and O^{2-} into the MnO_y film. During heat treatment, the film color changed from light brown to dark brown.

Fig. 10.8 HAADF-STEM image of the $Na_{\approx 2/3}MnO_2$/ α-Al_2O_3 substrate interface. Incident direction of the electron beam is $[1\bar{1}00]$ $Na_{\approx 2/3}MnO_2$. The atomically sharp heterointerface is clearly seen. Reprinted with permission from [45]. © 2017 ACS

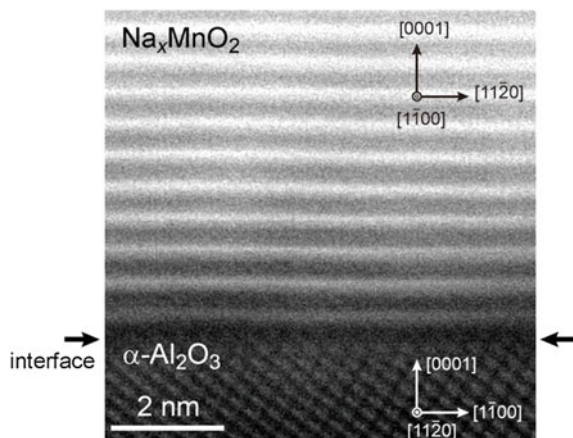**Fig. 10.9** Electrical conductivity. Temperature dependence of the electrical conductivity for the $Na_{\approx2/3}MnO_2$ and the $Na_{\approx0.61}MnO_2 \approx 0.42H_2O$ films measured by the AC impedance method in air. The resultant films show electrical conductivities of ~1 mS cm^{-1} for $Na_{\approx2/3}MnO_2$ film and ~0.1 mS cm^{-1} for $Na_{\approx0.61}MnO_2 \approx 0.42H_2O$ film at RT. Inset shows the σT–$1/T$ plots for both films; the activation energy (E_a) for electron hopping conduction is 0.47 eV. Reprinted with permission from [45]. © 2017 ACS
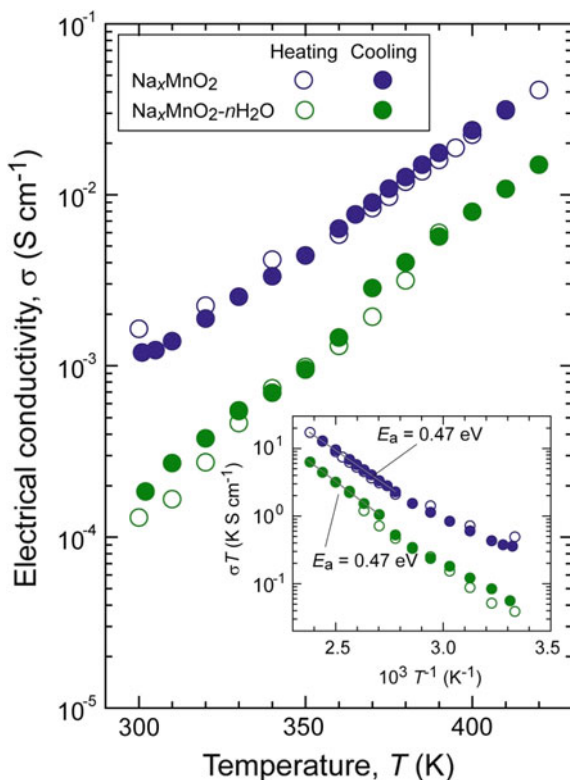

Figure 10.8 shows a cross-sectional HAADF-STEM image of the R-SPE grown $Na_{\approx2/3}MnO_2$ film around the interface observed from the direction of $Na_{\approx2/3}MnO_2\|\alpha$-$Al_2O_3$. The stripe patterns correspond to the layered structure of $Na_{\approx2/3}MnO_2$. It should be noted that an interfacial layer is not observed, confirming that the present sample has an atomically sharp interface between the film and substrate, contrary to the previously reported observation for a $Na_{\approx0.8}CoO_2$ film.

Figure 10.9 summarizes the temperature (T) dependence of the electrical conductivity (σ) for the $Na_{\approx2/3}MnO_2$ and hydrated $Na_{\approx0.61}MnO_2 \approx 0.42H_2O$ epitaxial films. It should be noted that the $\sigma - T$ curves for both films do not show a remarkable hysteresis in the heating–cooling cycles ranging from RT to 400 K, suggesting that the absorbed water does not significantly contribute to σ because the surface-adsorbed water should be released at 100–150 °C, although a slight deviation from a straight line at ~100 °C is observed in hydrated $Na_{\approx0.61}MnO_2 \approx 0.42 H_2O$ film. At RT, σ of the $Na_{\approx2/3}MnO_2$ epitaxial film is ~1 mS cm^{-1}, which is two orders of magnitude larger than that of an α-$Na_{0.70}MnO_{2.25}$ single crystal (~0.5 μS cm^{-1}). In contrast, σ of the $Na_{\approx0.61}MnO_2 \approx 0.42H_2O$ film is ~0.1 mS cm^{-1}, which is comparable to that of the $Na_xMnO_2 \cdot nH_2O$ ceramic (~0.05 mS cm^{-1}). In both cases, σ increases exponentially with temperature because electron hopping becomes

faster at higher temperatures. The activation energy for electron hopping (E_a) observed for both films in the 300–400 K range is 0.47 eV, which is comparable to those of other Mn^{3+}/Mn^{4+}-containing oxides, such as α-$MnO_{2-\delta}$, Li_xMnO_2, and $LiMn_2O_4$. In contrast to $Na_{\approx 0.35}CoO_2 \cdot 1.3H_2O$, the electron hopping conductivity of $Na_{\approx 2/3}MnO_2$ decreases by the hydration treatment. This decrease is most likely because the intercalated water molecules affect the ratio of Mn^{3+}/Mn^{4+}.

### 10.3.2 $Li_4Ti_5O_{12}$ Epitaxial Film

$Li_4Ti_5O_{12}$ (S.G. $Fd\overline{3}m$) is one of the most promising anode active materials of solid Li-batteries, [46, 47] due to its structural stability during charge/discharge reactions [48] with excellent reversibility [49, 50] and a long cycle life [51]. Although epitaxial film growth of $Li_4Ti_5O_{12}$ by PLD has been reported, [52, 53] the target ceramic containing excess Li species is required to fabricate stoichiometric $Li_4Ti_5O_{12}$ thin films. On the contrary, Li et al. fabricated an amorphous $Li_4Ti_5O_{12}$ film by PLD on a (001) $SrTiO_3$ single-crystal substrate at room temperature with a stoichiometric $Li_4Ti_5O_{12}$ target, and heated the amorphous film with molten $LiNO_3$ at 600 °C in air. As a result of this "solid–liquid phase epitaxy", they successfully fabricated an epitaxial film of single-phase $Li_4Ti_5O_{12}$ [54].

The solid–liquid phase epitaxy procedure for the growth of $Li_4Ti_5O_{12}$ films is schematically illustrated in Fig. 10.10. Step 1(a): Amorphous Li-Ti-O films (100 nm thick) are deposited at RT on (001) $SrTiO_3$ single-crystal substrates (area: 10×10 mm^2, thickness: 0.5 mm) by PLD. The in-plane lattice mismatch is too large for $Li_4Ti_5O_{12}$ to coherently grow on (001) $SrTiO_3$ substrate, where the lattice mismatch between cubic $Li_4Ti_5O_{12}$ (the half of a-axis lattice parameter, $a/2 = 0.4176$ nm) and $SrTiO_3$ ($a = 0.3905$ nm) is estimated to be −6.9%. A KrF excimer laser with an energy fluence of ∼2 J cm^{-2} pulse^{-1} and a repetition rate of 10 Hz is used to ablate a ceramic target of stoichiometric $Li_4Ti_5O_{12}$. The oxygen pressure during film deposition is kept at a low P_{O2} of 1.0×10^{-3} Pa and the deposition rate is 3.3 nm min^{-1}. Step 2(b): The resultant film is covered with $LiNO_3$ powder. Then it is heated at 600 °C for 30 min in air at temperature increasing rate of 40 °C/min in an Al_2O_3 crucible using an electric furnace. During the heating process, the $LiNO_3$ powder melts due to its low melting point of 261 °C and entirely covers the Li-Ti-O film at 600 °C. The film is naturally cooled to RT in the furnace. Step 3(c): The resultant film is washed by distilled water since the film surface is covered with the remaining $LiNO_3$ film. The resultant film surface looks very clean, indicating that $LiNO_3$ is successfully removed.

Figure 10.11a–c shows the out-of-plane XRD patterns for $Li_4Ti_5O_{12}$ films [(a) as-deposited, (b) heated at 600 °C without $LiNO_3$, and (c) heated at 600 °C with $LiNO_3$]. Only the intense diffraction peaks of 00 l $SrTiO_3$ are observed in the as-deposited $Li_4Ti_5O_{12}$ film, indicating that the film is amorphous (Fig. 10.11a).

Fig. 10.10 Solid–liquid phase epitaxy of the $Li_4Ti_5O_{12}$ film. **a** Step 1: An amorphous $Li_4Ti_5O_{12}$ film is deposited at RT on a (001) $SrTiO_3$ single-crystal substrate by PLD using a dense $Li_4Ti_5O_{12}$ ceramic as the target. **b** Step 2: The resultant film is heated at 600 °C for 30 min in air with a $LiNO_3$ powder, which melts during the heating process, in an Al_2O_3 crucible using electric furnace. Then the film is naturally cooled down to RT in the furnace. **c** Step 3: The $Li_4Ti_5O_{12}$ epitaxial film is obtained after the resultant film is washed with distilled water since the film surface is covered with remaining $LiNO_3$ film. Reprinted from [54]. © 2016 The Japan Society of Applied Physics
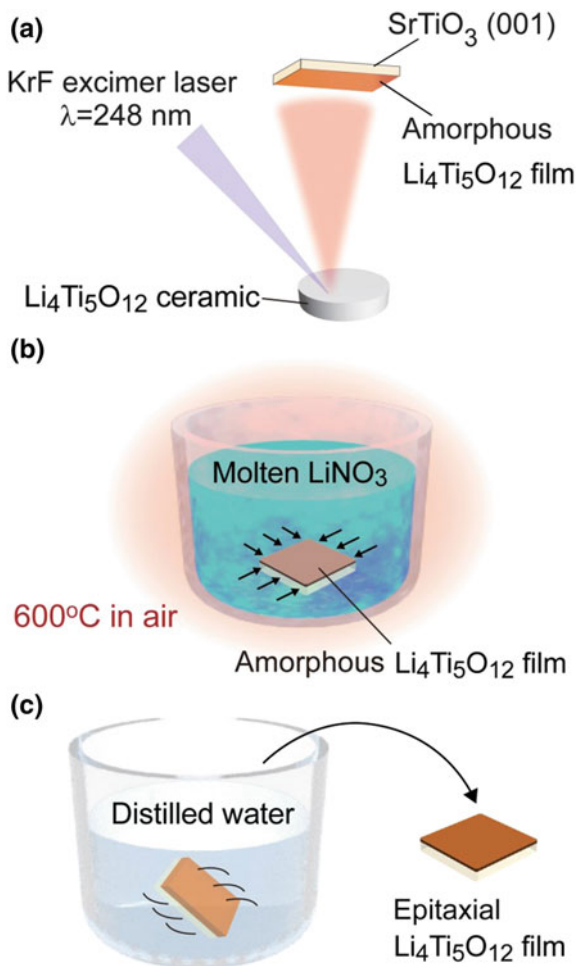
After heating the amorphous $Li_4Ti_5O_{12}$ film without $LiNO_3$ powder at 600 °C in air, the 004 anatase-TiO_2 diffraction peak is observed, but the $Li_4Ti_5O_{12}$ diffraction peak is not seen in the out-of-plane XRD pattern (Fig. 10.11b). The c-axis lattice parameter (0.954 nm) for the TiO_2 phase is almost the same as 0.951 nm for the pure anatase-TiO_2 bulk [55].

In contrast, the intense diffraction peak of 004 $Li_4Ti_5O_{12}$ is observed after the film is heated with molten $LiNO_3$ at 600 °C (Fig. 10.11c). The full width at half maximum (FWHM) value of the out-of-plane rocking curve ($\Delta\omega$) for 004 $Li_4Ti_5O_{12}$ diffraction is ~0.8°, indicating that the $Li_4Ti_5O_{12}$ film is preferentially oriented perpendicular to the substrate surface (Fig. 10.11d). The chemical composition of the $Li_4Ti_5O_{12}$ film could not be accurately estimated when the Li/Ti ratio is an extremely large value of ~5.0, presumably due to the residual adhesive $LiNO_3$
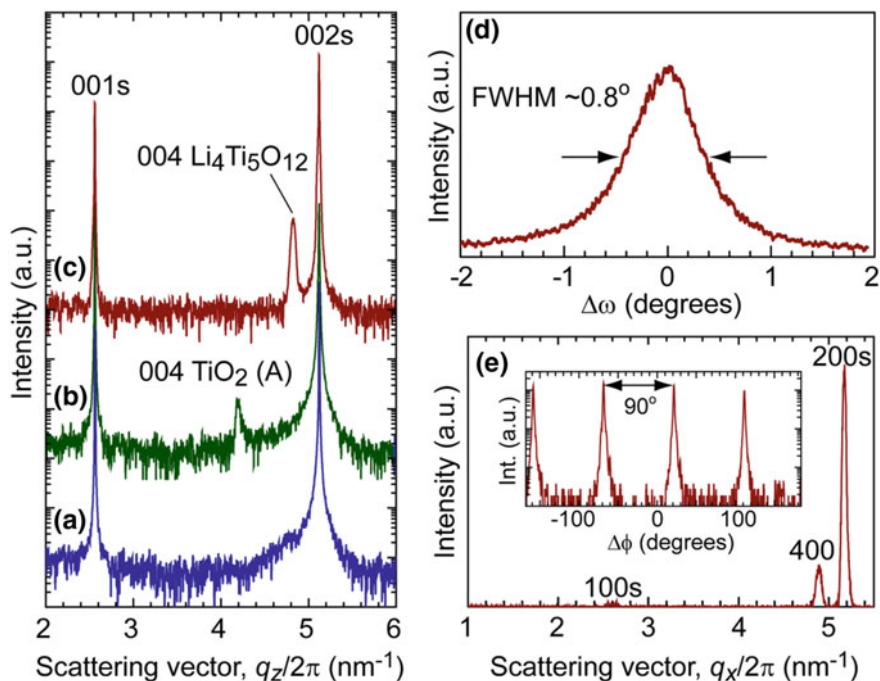
Fig. 10.11 Out-of-plane XRD patterns of the $Li_4Ti_5O_{12}$ films [**a** as-deposited, **b** heated at 600 °C without $LiNO_3$ (solid-phase epitaxy), **c** heated at 600 °C with $LiNO_3$ (solid–liquid phase epitaxy)]. Only intense diffraction peaks of 00 *l* $SrTiO_3$ are seen in the as-deposited $Li_4Ti_5O_{12}$ film (**a**), indicating that the as-deposited film is amorphous. The intense diffraction peak of 004 $Li_4Ti_5O_{12}$ is observed in (**c**), although 004 anatase TiO_2 is crystallized when the film is heated without $LiNO_3$ powder (**b**). FWHM of the Xray rocking curve ($\Delta\omega$) for the 004 $Li_4Ti_5O_{12}$ is ~0.8° (**d**). **e** In-plane XRD pattern of the $Li_4Ti_5O_{12}$ film grown by solid–liquid phase epitaxy. Only the intense diffraction peak of 400 $Li_4Ti_5O_{12}$ is seen together with *h*00 $SrTiO_3$. The ϕ scan of 400 $Li_4Ti_5O_{12}$ diffraction [(**e**) inset] shows a fourfold rotational symmetry with every 90° rotation originating from the cubic symmetry of $Li_4Ti_5O_{12}$ lattice. Reprinted from [54]. © 2016 The Japan Society of Applied Physics

and/or Li species incorporated into $SrTiO_3$ substrate. However, the film density characterized by the Xray reflectivity measurements for the $Li_4Ti_5O_{12}$ film is 3.5 g cm^{-3}, which is consistent with the 3.48 g cm^{-3} of the $Li_4Ti_5O_{12}$ phase. In contrast, that of the $Li_4Ti_5O_{12}$ film heated without $LiNO_3$ is 4.1 g cm^{-3}, approaching 3.90 g cm^{-3} of the anatase TiO_2 due to the decrease of in Li content in the film. At this stage, the actual vaporization temperature of Li in the $Li_4Ti_5O_{12}$ film has yet to be examined, but these results suggest that molten $LiNO_3$ plays an essential role in suppressing the vaporization of Li species and enables crystallization of the $Li_4Ti_5O_{12}$ phase at relatively low temperature (600 °C) by solid–liquid phase epitaxy.

10.3.3 KFe_2As_2 Epitaxial Film

A novel attractive property has recently been theoretically predicted for KFe_2As_2. Pandey et al. [56] reported that KFe_2As_2, which is the end member of the 122-type iron-based superconductors $(Ba_{1-x}K_x)$ Fe_2As_2 (i.e., $x = 1$) with a critical temperature ≈ 3 K [57], may exhibit a large spin Hall conductivity (SHC), which is comparable to that of Pt [58]. That is, it exhibits 10^4 times larger SHC (2×10^4 Ω^{-1} m^{-1}) than that of a semiconductor (0.5 Ω^{-1} m^{-1}) [59]. Such a high SHC originates from the strong spin-orbit coupling of the Fe 3d states with Dirac cones below the Fermi level of heavily hole-doped KFe_2As_2. Indeed, high-resolution angle-resolved photoemission spectroscopy experiments show that the electron pocket at the M point of $(Ba_{1-x}K_x)Fe_2As_2$ completely disappear for KFe_2As_2 due to its heavily self-hole-doped nature ($Ba^{2+} \leftrightarrow K^+ +$ hole) [60].

Because KFe_2As_2 contains alkali metal K as its main constituent, it is very air sensitive. Therefore, the thin-film growth of KFe_2As_2 is difficult due to two intrinsic properties: its extremely hygroscopic nature and the high vapor pressure of potassium. Thin-film growth of KFe_2As_2 and electrical measurements with device patterning are challenging issues. These issues were solved by combining room-temperature pulsed laser deposition using K-rich KFe_2As_2 bulk targets with thermal crystallization in a KFe_2As_2 powder after encapsulation in an evacuated silica-glass tube. All of the setup processes must be conducted in a vacuum chamber and a dry Ar atmosphere in a glove box (Fig. 10.12) [61]. Optimized KFe_2As_2 films on (La, Sr)(Al, Ta)O_3 single-crystal substrates are obtained by crystallization at 700 °C. These films are strongly c-axis oriented. Electrical measurements were performed with thin films protected by grease passivation to block reaction with the atmosphere. The KFe_2As_2 films exhibit a superconductivity transition at 3.7 K, which is the same as that of bulk KFe_2As_2. This result is the first demonstration of a superconducting KFe_2As_2 thin film.

The obtained KFe_2As_2 films are, however, not epitaxial films, but c-axis orientated ones without an in-plane orientation. This is attributed to the maximum thermal annealing temperature up to 700 °C in the conventional annealing method sealed in an evacuated silica-glass tube. When we raised the annealing temperature to >700 °C, the films decompose into Fe_2As, FeAs, and Fe. It indicates that the gas-tightness of this synthesis condition is poor >700 °C for K and the alkali metal component K does not remain in the films.

Therefore, an improved solid-phase epitaxy technique using a custom-made alumina vessel, which realizes a high annealing temperature of 1000 °C without vaporization of K from the films, was developed, and high-quality heteroepitaxial KFe_2As_2 thin films on MgO single crystals were successfully obtained (Fig. 10.13) [62]. This result demonstrates that this solid-phase epitaxy technique is a powerful method for the complex compounds with extremely high vapor pressures, such as K.
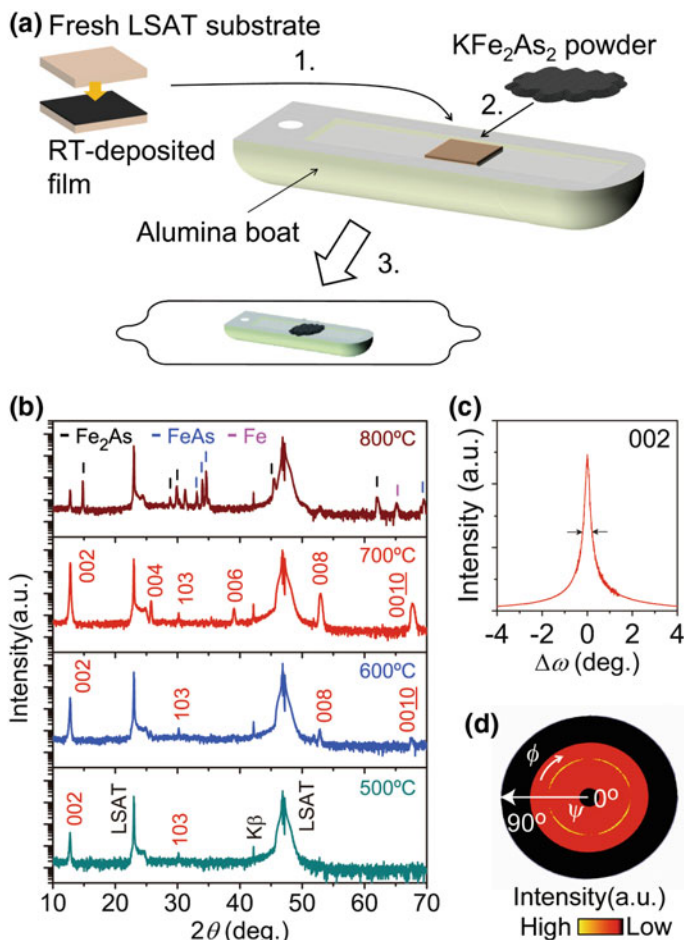
Fig. 10.12 Solid-phase epitaxy for KFe$_2$As$_2$ film growth. **a** Set up before thermal annealing. **b** XRD patterns of the films annealed at T_a = 500–800 °C buried in KFe$_2$As$_2$ powder. **b** Out-of-plane rocking curve of the 002 diffraction of the KFe$_2$As$_2$ film annealed at T_a = 700 °C. **c** Pole figure of the 103 diffraction of the KFe$_2$As$_2$ film annealed at T_a = 700 °C. Reprinted from ref. [61]. Copyright © 2014 American Chemical Society

10.3.4 (Sn, Pb)Se Epitaxial Film

SnSe is usually a p-type semiconductor and has the orthorhombic GeS-type layered crystal structure composed of an alternating stack of (Sn^{2+}Se^{2-})$_2$ layers along the *a*-axis. In contrast, a simple binary selenide PbSe has a cubic rock-salt (RS-) type structure. Different from SnSe, the RS-type structure is thermodynamically stable for PbSe at room temperature. Comparing these crystal structures, one expects that a smaller hole effective mass and a higher hole mobility would be realized if the
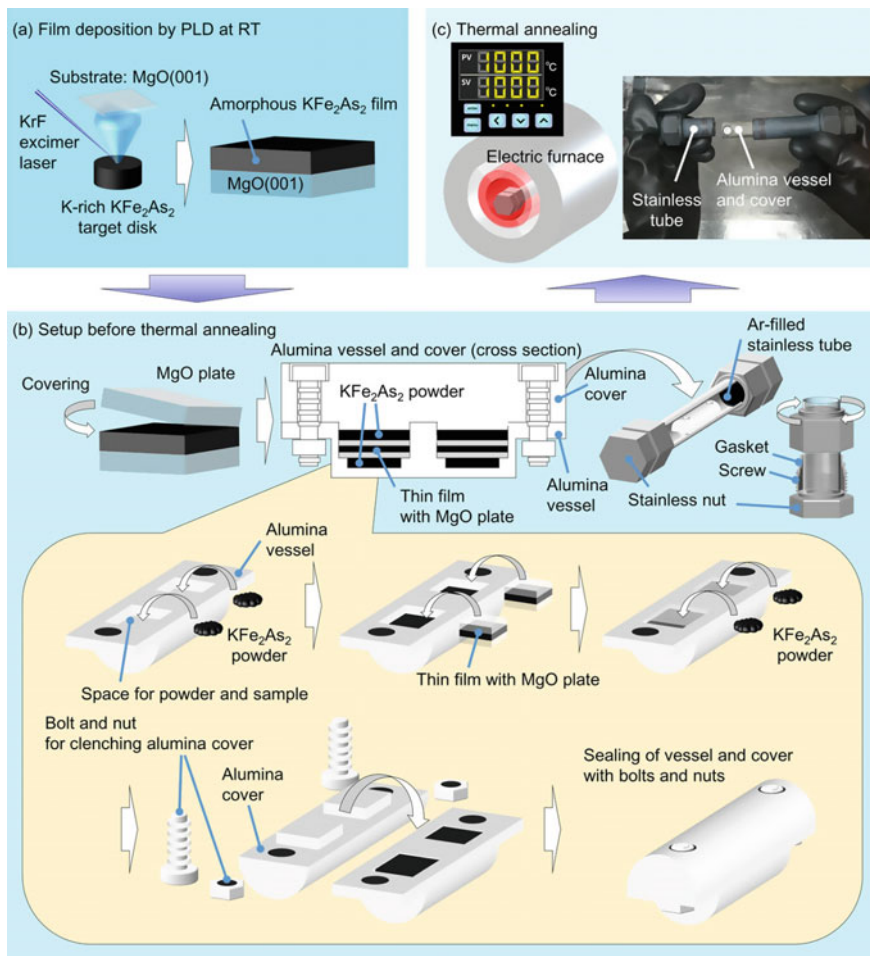
Fig. 10.13 Improved solid-phase epitaxy for KFe_2As_2 film growth. Reprinted from ref. [62]. Copyright © 2016 The Japan Society of Applied Physics

crystal structure of SnSe is changed from the thermal equilibrium GeS-type one to the RS-type one because the three-dimensional network of high-coordination number polyhedra [sixfold ($PbSe_6$) in the RS-type one] forms larger band dispersions than two-dimensional layered structures [threefold ($SnSe_3$) in the GeS-type one]. As found in the SnSe–PbSe phase diagram, isovalent Pb^{2+} ions can substitute for part of the Sn^{2+} sites in the orthorhombic GeS-type SnSe at thermal equilibrium [63]. For example, at 400 K, ~20% Pb^{2+} can occupy the Sn^{2+} sites in the orthorhombic GeS-type structure, while more than 60% Pb^{2+} substitution is necessary to stabilize the RS-type structure in (Sn, Pb)Se. On the other hand, in the intermediate Pb concentration region between 20 and 60%, single-phase (Sn, Pb)Se

is not obtained. Only a mixture of the GeS-type and the RS-type phases is obtained at a thermal equilibrium at 400 K. However, the RS-type (Sn, Pb)Se with smaller Pb concentrations down to ~40% is stabilized at higher temperatures (e.g., ~1100 K).

Recently, RS-type SnSe and (Sn, Pb)Se have gathered renewed attention because they are expected to be new topological insulators. So far, RS-type (Sn, Pb)Se single crystals are grown using a self-selecting vapor-growth method by a large amount of Pb doping to SnSe (63 and 77% Pb doping) [i.e., the chemical compositions are very Pb-rich, $(Sn_{0.37}Pb_{0.63})Se$ and $(Sn_{0.23}Pb_{0.77})Se$.] Although a higher Sn concentration would provide a higher topological insulator transition temperature, the maximum Sn concentration is limited to 37%, corresponding to a minimum Pb concentration as high as 63% to stabilize the cubic RS-type structure in SnSe. From the phase diagram, the RS-type (Sn, Pb)Se composition region by freezing the high-temperature RS-type (Sn, Pb)Se phase may be extended.

Thus, isovalent Pb doping to the orthorhombic GeS-type SnSe in order to stabilize the nonequilibrium RS-type (Sn, Pb)Se phase was examined. Reactive solid-phase epitaxy [29], in which a thin RS-type PbSe epitaxial template layer works as a sacrificial layer (Fig. 10.14), was employed [64]. Additionally, a quenching process from 600 °C to RT also effectively stabilizes the nonequilibrium RS-type epitaxial (Sn, Pb)Se. Using this technique, we succeeded in varying the Pb concentration from 0 to 100%. The minimum Pb concentration to stabilize the RS-type SnSe is 50%, which is the lowest minimum Pb content ever reported. A structural transition from the GeS-type to the RS-type drastically increases the hole mobility from 60 for SnSe to 290 cm^2 V^{-1} s^{-1} for 58% Pb-doped RS-type film, as expected. The p-type to n-type conversion is also observed upon further increasing the Pb doping up to 100% (i.e., the end member PbSe). A maximum electron mobility of 340 cm^2 V^{-1} s^{-1} is achieved by 61% Pb doping.

10.4 Modulation of Functional Nanolayers

State-of-the-art information storage devices such as USB flash drives are electronic data storage devices, which store digital information by electrical resistivity changes of semiconducting silicon using the electric field effect to process information into "words" consisting of various combinations of the numbers "0" and "1". Since miniaturization technology has already reached its limit, epoch-making technology is strongly required to further improve the storage capacity.

We have demonstrated multi-information memory devices, which are composed of metal oxides showing both an electrical resistivity change and magnetism/color change simultaneously by a redox reaction of the metal oxides. Three-terminal thin-film transistor (TFT) structures were fabricated on a functional metal oxide using an insulating oxide, water-infiltrated calcium aluminate (C12A7) with
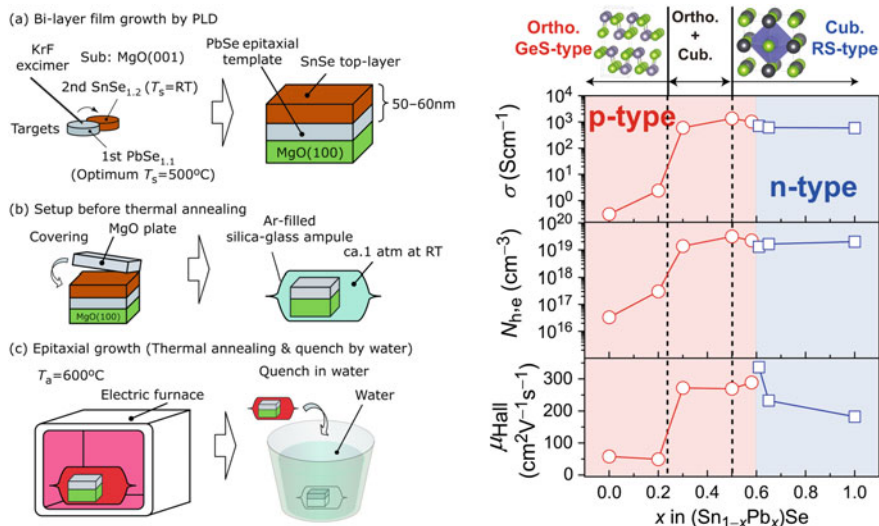
Fig. 10.14 Reactive solid-phase epitaxy for the $(Sn_{1-x}Pb_x)S$ epitaxial films and their carrier transport properties at room temperature as a function of x. σ, $N_{h,e}$, and μ_{Hall} show the electrical conductivity, carrier concentration of hole or electron, and Hall mobility, respectively. Reprinted from ref. [64]. Copyright © 2016 American Chemical Society

mesoporous structure, as the gate insulator. We utilized H^+/OH^- ions in the water to change the valence state of the metal oxides by applying a gate voltage since H^+/OH^- ions are strong reducing/oxidizing agents for metal oxides. Upon changing the valence of the transition metal ion, the metal oxide changes from an insulator to a metal as well as from nonmagnetic to magnetic or from colorless transparent (invisible) to visible, as schematically illustrated in Fig. 10.15. Although the present device requires a relatively long storage time (a few seconds) because it utilizes mobile ion diffusion in the functional metal oxide, it has great merits. For example, it has nonvolatile operations, which mean no standby power is required after storing information. The present multi-information storage device should be useful for Internet of Things (IoT) technologies.

As IoT technologies become more ubiquitous, the information gathered annually is rapidly increasing as various machines, as well as personal computers, are connected to the internet. State-of-the-art information storage devices such as USB flash drives are electronic data storage devices. They store digital information using an electrical resistivity change of semiconducting silicon and an electric field effect that process information into "words" consisting of various combinations of the numbers "0" and "1". Although the storage capacity of such devices increased annually due to miniaturization techniques, the limit of such miniaturization techniques has already been reached. Consequently, complicated multi-levelization techniques such as "0", "1", "2", and "3" are utilized to improve the storage
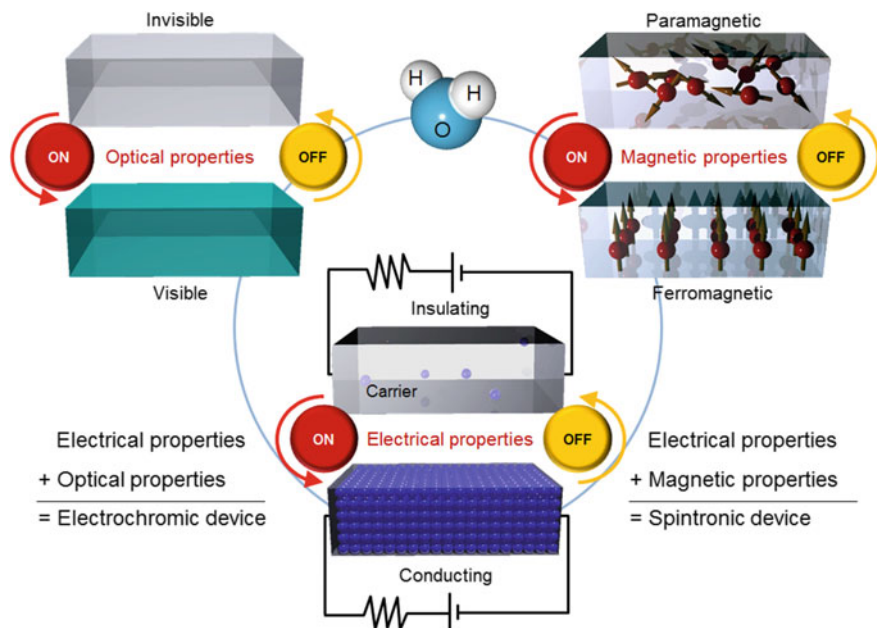
Fig. 10.15 Schematic concept of a reversible conversion of optical-, electrical-, and magnetic properties of functional metal oxides using an electrochemical redox reaction of metal oxides with H^+ and OH^- of liquid water. For example, by combining the electrical properties and the optical properties, a novel electrochromic device, which can store A/B in addition to 0/1 for storing information, can be developed

capacity. To further improve the storage density, epoch-making technology is strongly required.

To overcome this obstacle, we proposed the following idea: utilizing functional materials whose optical transmittance or magnetism can be dramatically changed together with a change in the electrical resistivity. Such features would be very useful to improve the storage capacity. For example, multiple storing/reading of information becomes possible when vision and electrical signals are combined with displays. Such devices are appropriate for future IoT technologies. However, it is impossible to use optical transmittance or magnetic properties in case of semiconductor Si. In addition, it is impossible to use the electrical resistivity change in case of a magnetic metal.

Our research has focused on metal oxides because some metal oxides exhibit changes in their optical property or magnetic property together with the electrical property via an oxidation/reduction (redox) reaction. Generally, such redox reactions occur at a high temperature (several hundred degrees) heat treatment in an oxidizing or reducing atmosphere. However, this method is inappropriate for device operations. On the other hand, redox reactions using electrochemistry such

chemical battery cells occur at room temperature. The latter technique is appropriate for practical applications, but the device must be sealed to prevent electrolyte leakage.

Unexpectedly, in 2010, Ohta et al. found that water, which is automatically absorbed into the mesoporous structure of an insulating oxide due to capillary action, can be a good electrolyte for this purpose [65]. Three-terminal thin-film transistor (TFT) structures were fabricated on a functional metal oxide using an insulating oxide, calcium aluminate ($12CaO \bullet 7Al_2O_3$, C12A7) with mesoporous structure (namely CAN, calcium aluminate with nanopores) as the gate insulator (Fig. 10.16). C12A7 can be prepared by PLD at room temperature under a relatively high oxygen atmosphere of ~5 Pa. CAN films contain many mesopores (~10 nm in diameter) whose volume fraction is ~30% [65]. Temperature desorption spectra of the CAN film reveal that the mesopores are fully occupied with molecular water. The AC conductivity of the CAN film is ~10^{-9} S cm^{-1} at room temperature, [66] which is comparable to that of ultrapure water. Thus, water moisture in air is automatically absorbed in the mesopores of CAN film by capillary action.

In 2016, Katase and Ohta et al. utilized H^+/OH^- ions in a water-infiltrated CAN film to change the valence of the metal oxides by applying a gate voltage because H^+/OH^- ions are strong reducing/oxidizing agents for metal oxides. As the valence of the transition metal ion changes, the metal oxide changes from an insulator to a metal, a nonmagnetic to a magnetic material, or from transparent to a black color. Although the present device requires a relatively long storage time (a few seconds) since it utilizes mobile ion diffusion in the functional metal oxide, it has great merits. For example, it has nonvolatile operations, which mean no standby power is required after storing information. The present multi-information storage devices would be useful for IoT technologies.

The authors have developed two multi-information memory devices, which use a magnetic [67] or optical [68] signal along with an electronic signal to double the storage capacity in these "multiplex writing/reading" devices. In addition to the binary 0/1 method of storing information in a state-of-the-art memory device, the present devices can also store A/B for the information. More details for each type of memory device are provided below.

10.4.1 Utilizing Antiferromagnetic Insulator/Ferromagnetic Metal Conversion in SrCoO$_{2.5+\delta}$ [67]

To realize "multiplex writing/reading" devices, material selection is the most information factor. Katase and Ohta et al. choose strontium cobaltite, SrCoO$_{2.5+\delta}$, for this purpose because SrCoO$_{2.5}$ is an antiferromagnetic insulator and SrCoO$_3$ is a ferromagnetic metal [69, 70]. The valence state of the cobalt ion in SrCoO$_{2.5+\delta}$ can be controlled from 3 + (SrCoO$_{2.5}$) to 4 + (SrCoO$_3$) by changing the excess oxygen
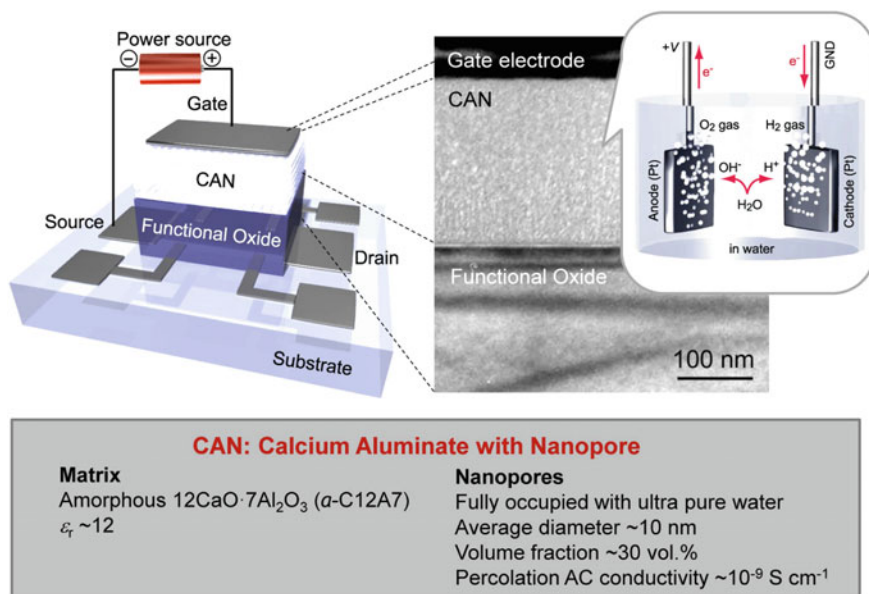
Fig. 10.16 Schematic illustration of CAN (calcium aluminate with nanopore) gated functional oxide thin-film transistor with a three-terminal electrodes geometry. Since 30 volume percent of the CAN film is occupied with liquid water, H^+ and OH^- ions in the CAN film move with a gate voltage application. The percolation AC conductivity is $\sim10^{-9}$ S cm^{-1}, which is comparable to that of ultrapure water. Changing the valence of the transition metal ion by a gate voltage application changes the functional oxide from an insulator to a metal as well as from a nonmagnetic to a magnetic material or from colorless and transparent to a black color

content (δ) from 0 to 0.5. Since the crystal structures of $SrCoO_{2.5}$ (brownmillerite) and $SrCoO_3$ (perovskite) are similar, the authors expected that the topotactic redox reaction between $SrCoO_{2.5}$ and $SrCoO_3$ can be controlled electrochemically. By utilizing this phenomenon for three-terminal thin-film transistors with water containing a mesoporous glass gate insulator, we developed a multi-information memory device. This device can be utilized not only to change the electrical resistivity (0/1) but also to change of magnetic property (A/B), as schematically shown in Fig. 10.17.

The three-terminal TFT device, which is composed of an epitaxial $SrCoO_{2.5}$ film (30 nm, active channel material), an amorphous Na-Ta-O film with a mesoporous structure (300 nm, gate insulator), and an amorphous WO_3 film (20 nm, proton absorber), was prepared by PLD on (001) $SrTiO_3$ single-crystal substrate. It should be noted that we recently developed an amorphous Na-Ta-O film with a mesoporous structure, which can be used as an alkaline solution. When a negative gate voltage (-3 V) is applied between the gate and source electrodes, OH^- ions, which are contained in the mesoporous glass, penetrate into $SrCoO_{2.5+\delta}$. Finally, $SrCoO_3$

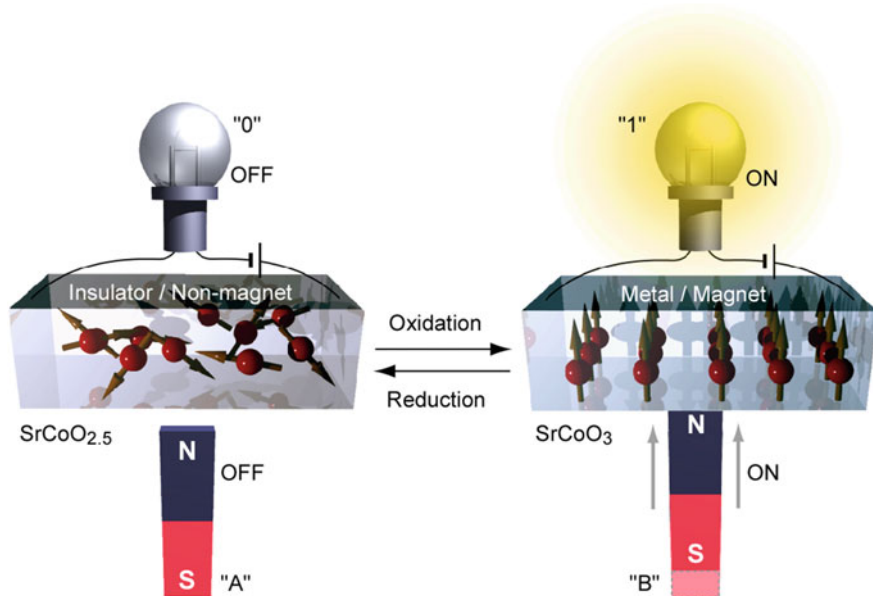**Fig. 10.17** Principle of a multi-memory device using antiferromagnetic insulator/ferromagnetic metal conversion in $SrCoO_{2.5+\delta}$. This device would store both A/B and 0/1 information. Reprinted with permission from [67]. © 2016 John Wiley and Sons

is formed in 3 s. On the contrary, a positive gate voltage (+3 V) application to the gate–source electrodes reduces $SrCoO_3$ into $SrCoO_{2.5}$ in 3 s [67].

Figure 10.18a shows a schematic of the device structure, which is similar to conventional three-terminal thin-film transistors. The channel (source–drain) length and width are 800 μm and 400 μm, respectively. The electrodes E1–E4 are used to measure the sheet resistance (R_s). Figure 10.18b shows the changes in R_s of the device. Before the device operation (state A), R_s increases with decreasing temperature, indicating an insulating behavior. When a negative gate voltage (−3 V) is applied for 3 s (state B), R_s decreases by three orders of magnitude and shows a metallic temperature dependence. After that, the device returns to the original state when a positive gate voltage (+3 V) is applied for 3 s. The device is reversibly operable (Fig. 10.18b, inset).

Figure 10.18c shows the changes in the magnetic state of the device at states A, B, and C. At states A and C, the magnetic moment is zero, indicating that $SrCoO_{2.5+\delta}$ ($\delta = 0$) is an antiferromagnetic state. At state B, the device shows a ferromagnetic behavior with a Curie temperature of 275 K, indicating that $SrCoO_{2.5+\delta}$ ($\delta \sim 0.5$) is a ferromagnetic state. These results clearly demonstrate that both electrical resistivity and magnetism changes can be used in the present device.
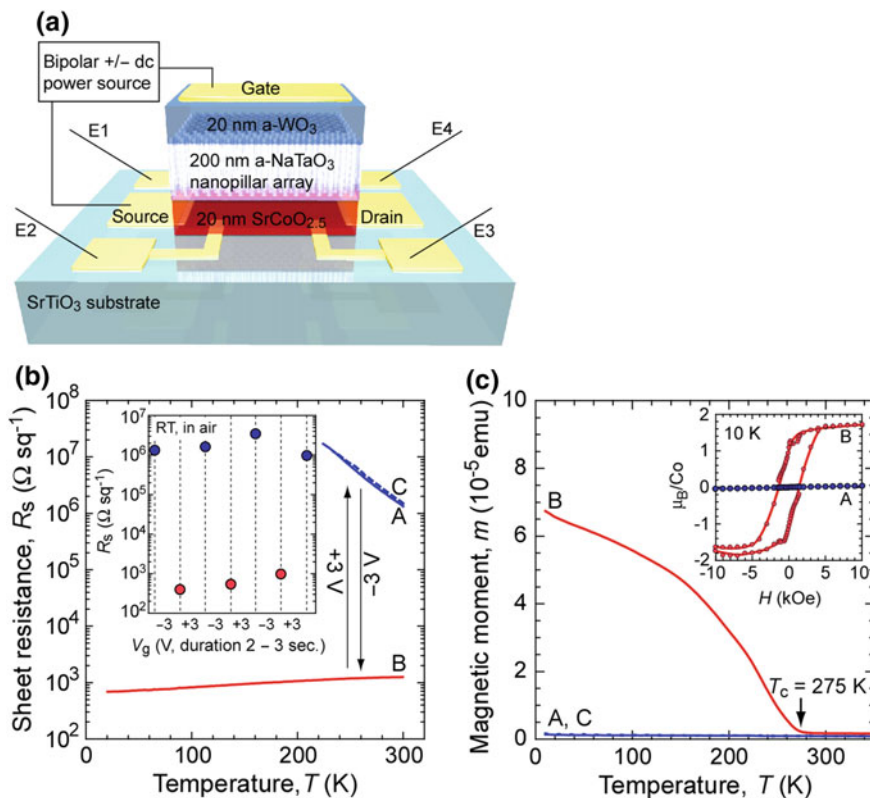
Fig. 10.18 a Schematic device structure similar to conventional three-terminal thin-film transistors. **b** Temperature dependence of the sheet resistance of the device. **a** Virgin state, **b** after applying a negative V_g of -3 V, and **c** subsequent application of $+3$ V (dotted line). The inset shows the cyclability at RT in air. **c** $m-T$ curves of the SrCoOx layer at states A−C in (**b**) measured under $H = 20$ Oe applied parallel to the in-plane direction. The inset shows a magnetic hysteresis loop at 10 K at states A and B. Reprinted with permission from [67]. © 2016 John Wiley and Sons

10.4.2 Utilizing a Colorless Transparent Insulator/Dark Blue Metal Conversion in H$_x$WO$_3$ [68]

Katase and Ohta et al. [68] have also developed a new information display/storage device using a three-terminal thin-film transistor structure on an electrochromic material, which has been attracted attention as an "electric curtain". The device shows a color change (colorless transparent/dark blue) together with an electrical conductivity change (insulator/metal) by applying a gate voltage. Since the device can be fabricated at room temperature, low cost fabrication is possible. Thus, larger area devices are easily fabricated. For example, the present device is applicable as an information display/storage on a window glass.

Protonation/deprotonation of tungsten trioxide (WO_3), known as an electrochromic material, is converted reversibly from a colorless transparent insulator to a dark blue metal [71]. By utilizing this phenomenon in a three-terminal thin-film transistor with a water-containing mesoporous glass gate insulator, a multi-information memory device has been realized. This device can be utilized using not only a change in the electrical resistivity (0/1) but also a change in optical transmittance (A/B), as schematically shown in Fig. 10.19.

The three-terminal TFT device composed of an amorphous WO_3 film (100 nm, active channel material), a mesoporous CAN film (300 nm, gate insulator), a polycrystalline NiO film (50 nm, oxygen absorber), and amorphous ITO films (20 nm, gate, source, and drain electrodes) was prepared by PLD at room temperature on a glass substrate. When a positive gate voltage (a few volts) is applied between the gate and the source electrodes, H^+ and OH^- ions, which are contained in the mesoporous glass, diffuse to the WO_3 and NiO sides, respectively, forming HWO_3 and NiOOH. Since the resultant dark blue colored HWO_3 shows a metallic electrical conductivity, the channel (drain–source) becomes electrically conductive. On the contrary, a negative gate voltage (a few volts) application to the gate–source electrodes results in HWO_3 and NiOOH returning to WO_3 and NiO, respectively. This conversion can be reversibly operated and the degree of change can be controlled by the applied gate voltage.

Figure 10.20a schematically depicts the device structure composed of a-WO_3 (80 nm), CAN (300 nm), and NiO (20 nm)/ITO (20 nm) layers. Transparent ITO thin films are used for all the electrodes. All the films are deposited by PLD at room temperature. The device was fabricated on a transparent glass substrate (1 cm × 1 cm) as shown in Fig. 10.20b. The channel (source–drain) length and
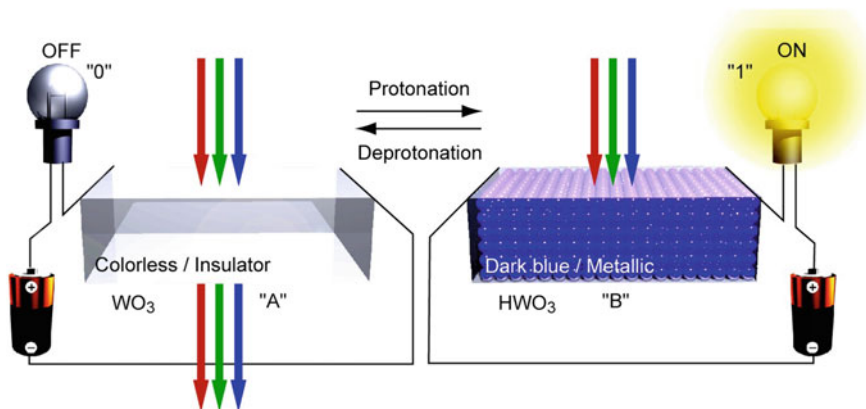

Fig. 10.19 Principle of a multi-memory device using a colorless transparent insulator (amorphous WO_3)/dark blue metal (amorphous HWO_3) conversion in H_xWO_3. This device would store both A/B and 0/1 information. This device should be suitable as a smart window or a smart mirror, which can display or store information. Furthermore, the present device can be used as an "electronic curtain" as the whole surface of window glass can be switched reversibly from colorless and transparent to dark blue. Reprinted from [68]. © 2016 NPG
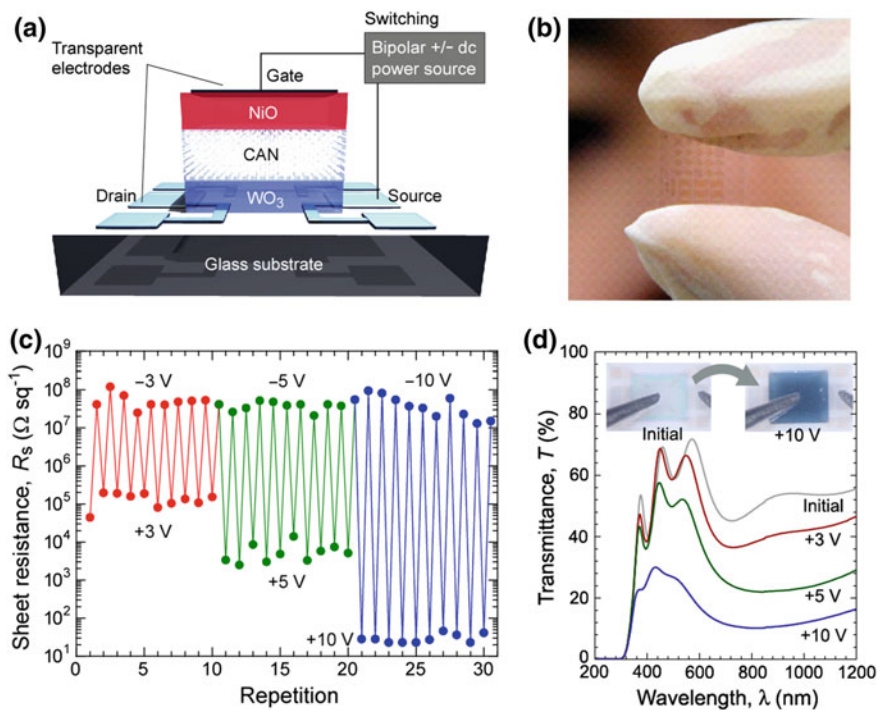
Fig. 10.20 **a** Schematic device structure. **b** Transparent device on a glass substrate. **c** Repeatable switching of the sheet resistance. **d** Optical transmission spectra. Before the operation, the device is an insulator ($R_s \sim 10^8 \ \Omega \ \text{sq}^{-1}$) and fully transparent in the visible light region. When a positive gate voltage is applied to the device for 10 s, R_s decreases several orders of magnitude and the device becomes dark blue due to electrochemical protonation of WO_3. Reprinted from [68]. © 2016 NPG

width are 800 μm and 400 μm, respectively. Note that the device is colorless and transparent. Figure 10.20c shows the changes in R_s. When a positive gate voltage is applied to the device for 10 s, R_s decreases by several orders of magnitude. The color becomes dark blue (Fig. 10.20d). The device reverts to the original state (transparent, insulator) when a negative gate voltage is applied for 10 s. The device is reversibly operable. Although the present device requires a relatively long storage time (a few seconds) since it utilizes mobile ion diffusion in the functional metal oxide, it has great merits. For example, it employs nonvolatile operation, which means standby power is not required after storing information. The present multi-information storage devices would be useful for IoT technologies.

References

1. R. Eason, *Pulsed Laser Deposition of Thin Films Applications-Led Growth of Functional Materials.* (Wiley, Inc., UK, 2007)
2. R. Ramesh, D.G. Schlom, MRS Bull. **33**, 1006 (2008)
3. H. Ohta, K. Sugiura, K. Koumoto, Inorg. Chem. **47**, 8429 (2008)
4. J.W. Fergus, J. Eur. Ceram. Soc. **32**, 525 (2012)
5. T. Okuda, K. Nakanishi, S. Miyasaka, Y. Tokura, Phys. Rev. B **63**, 113104 (2001)
6. S. Ohta, T. Nomura, H. Ohta, K. Koumoto, J. Appl. Phys. **97**, 034106 (2005)
7. H. Ohta, S. Kim, Y. Mune, T. Mizoguchi, K. Nomura, S. Ohta, T. Nomura, Y. Nakanishi, Y. Ikuhara, M. Hirano, H. Hosono, K. Koumoto, Nature Mater. **6**, 129 (2007)
8. H. Ohta, T. Mizuno, S.J. Zheng, T. Kato, Y. Ikuhara, K. Abe, H. Kumomi, K. Nomura, H. Hosono, Adv. Mater. **24**, 740 (2012)
9. W.S. Choi, H. Ohta, H.N. Lee, Adv. Mater. **26**, 6701 (2014)
10. P. Delugas, A. Filippetti, M.J. Verstraete, I. Pallecchi, D. Marre, V. Fiorentini, Phys. Rev. B **88**, 045310 (2013)
11. T.A. Cain, S. Lee, P. Moetakef, L. Balents, S. Stemmer, S.J. Allen, Appl. Phys. Lett. **100**, 161601 (2012)
12. I. Pallecchi, F. Telesio, D.F. Li, A. Fete, S. Gariglio, J.M. Triscone, A. Filippetti, P. Delugas, V. Fiorentini, D. Marre, Nature Commun. **6**, 6678 (2015)
13. S. Shimizu, S. Ono, T. Hatano, Y. Iwasa, Y. Tokura, Phys. Rev. B **92**, 165304 (2015)
14. L.D. Hicks, M.S. Dresselhaus, Phys. Rev. B **47**, 12727 (1993)
15. N.T. Hung, E.H. Hasdeo, A.R.T. Nugraha, M.S. Dresselhaus, R. Saito, Phys. Rev. Lett. **117**, 036602 (2016)
16. C. Rodenbucher, M. Luysberg, A. Schwedt, V. Havel, F. Gunkel, J. Mayer, R. Waser, Sci Rep-Uk **6**, 32250 (2016)
17. T. Tomio, H. Miki, H. Tabata, T. Kawai, S. Kawai, J. Appl. Phys. **76**, 5886 (1994)
18. L.F. Mattheiss, Phys. Rev. B **6**, 4718 (1972)
19. S.A. Turzhevsky, D.L. Novikov, V.A. Gubanov, A.J. Freeman, Phys. Rev. B **50**, 3200 (1994)
20. D. Oka, Y. Hirose, S. Nakao, T. Fukumura, T. Hasegawa, Phys. Rev. B **92**, 205102 (2015)
21. X.X. Xu, C. Randorn, P. Efstathiou, J.T.S. Irvine, Nature Mater. **11**, 595 (2012)
22. Y. Zhang, B. Feng, H. Hayashi, T. Tohei, I. Tanaka, Y. Ikuhara, H. Ohta, J. Appl. Phys. **121**, 185102 (2017)
23. R.D. Shannon, Acta Crystallogr. A **32**, 751 (1976)
24. Y. Ishida, R. Eguchi, M. Matsunami, K. Horiba, M. Taguchi, A. Chainani, Y. Senba, H. Ohashi, H. Ohta, S. Shin, Phys. Rev. Lett. **100**, 056401 (2008)
25. Y. Ikuhara, P. Pirouz, Microsc. Res. Tech. **40**, 206 (1998)
26. P.K. Davies, J.Z. Tong, T. Negas, J. Am. Ceram. Soc. **80**, 1727 (1997)
27. D.A. Muller, N. Nakagawa, A. Ohtomo, J.L. Grazul, H.Y. Hwang, Nature **430**, 657 (2004)
28. C.L. Chen, Z.C. Wang, F. Lichtenberg, Y. Ikuhara, J.G. Bednorz, Nano Lett. **15**, 6469 (2015)
29. H. Ohta, K. Nomura, M. Orita, M. Hirano, K. Ueda, T. Suzuki, Y. Ikuhara, H. Hosono, Adv. Funct. Mater. **13**, 139 (2003)
30. H. Ohta, H. Mizoguchi, M. Hirano, S. Narushima, T. Kamiya, H. Hosono, Appl. Phys. Lett. **82**, 823 (2003)
31. H. Hiramatsu, K. Ueda, H. Ohta, M. Orita, M. Hirano, H. Hosono, Appl. Phys. Lett. **81**, 598 (2002)

32. H. Ohta, S.W. Kim, S. Ohta, K. Koumoto, M. Hirano, H. Hosono, Cryst. Growth Des. **5**, 25 (2005)
33. K. Mizushima, P.C. Jones, P.J. Wiseman, J.B. Goodenough, Mater. Res. Bull. **15**, 783 (1980)
34. T. Ohzuku, A. Ueda, J. Electrochem. Soc. **141**, 2972 (1994)
35. I. Terasaki, Y. Sasago, K. Uchinokura, Phys. Rev. B **56**, 12685 (1997)
36. M. Lee, L. Viciu, L. Li, Y.Y. Wang, M.L. Foo, S. Watauchi, R.A. Pascal, R.J. Cava, N. P. Ong, Nature Mater. **5**, 537 (2006)
37. K. Takada, H. Sakurai, E. Takayama-Muromachi, F. Izumi, R.A. Dilanian, T. Sasaki, Nature **422**, 53 (2003)
38. R.E. Schaak, T. Klimczuk, M.L. Foo, R.J. Cava, Nature **424**, 527 (2003)
39. X.H. Ma, H.L. Chen, G. Ceder, J. Electrochem. Soc. **158**, A1307 (2011)
40. J. Billaud, R.J. Clement, A.R. Armstrong, J. Canales-Vazquez, P. Rozier, C.P. Grey, P.G. Bruce, J. Am. Chem. Soc. **136**, 17243 (2014)
41. J. Billaud, G. Singh, A.R. Armstrong, E. Gonzalo, V. Roddatis, M. Armand, T. Rojob, P.G. Bruce, Energy Environ. Sci. **7**, 1387 (2014)
42. R.O. Jean-Paul Parant, M. Devalette, C. Fouassier, P. Hagenmuller, J. Solid State Chem. **3**, 1 (1971)
43. A. Caballero, L. Hernan, J. Morales, L. Sanchez, J.S. Pena, M.A.G. Aranda, J. Mater. Chem. **12**, 1142 (2002)
44. S. Hirano, R. Narita, S. Naka, J. Cryst. Growth **54**, 595 (1981)
45. S. Katayama, T. Katase, T. Tohei, B. Feng, Y. Ikuhara, H. Ohta, Cryst. Growth Des. **17**, 1849 (2017)
46. K. Zaghib, M. Simoneau, M. Armand, M. Gauthier, J. Pow. Sources **81**, 300 (1999)
47. G.X. Wang, D.H. Bradhurst, S.X. Dou, H.K. Liu, J. Pow. Sources **83**, 156 (1999)
48. F. Ronci, P. Reale, B. Scrosati, S. Panero, V.R. Albertini, P. Perfetti, M. Di Michiel, J.M. Merino, J. Phys. Chem. B **106**, 3082 (2002)
49. S. Scharner, W. Weppner, P. Schmid-Beurmann, J. Electrochem. Soc. **146**, 857 (1999)
50. M. Kitta, T. Akita, Y. Maeda, M. Kohyama, Langmuir **28**, 12384 (2012)
51. K.M. Colbow, J.R. Dahn, R.R. Haering, J. Pow. Sources **26**, 397 (1989)
52. M. Hirayama, K. Kim, T. Toujigamori, W. Cho, R. Kanno, Dalton T **40**, 2882 (2011)
53. A. Kumatani, T. Ohsawa, R. Shimizu, Y. Takagi, S. Shiraki, T. Hitosugi, Appl. Phys. Lett. **101** (2012)
54. N. Li, T. Katase, Y. Zhu, T. Matsumoto, T. Umemura, Y. Ikuhara, H. Ohta, Appl. Phys. Express **9** (2016)
55. J.K. Burdett, T. Hughbanks, G.J. Miller, J.W. Richardson, J.V. Smith, J. Am. Chem. Soc. **109**, 3639 (1987)
56. S. Pandey, H. Kontani, D.S. Hirashima, R. Arita, H. Aoki, Phys. Rev. B **86** (2012)
57. K. Sasmal, B. Lv, B. Lorenz, A.M. Guloy, F. Chen, Y.Y. Xue, C.W. Chu, Phys. Rev. Lett. **101** (2008)
58. T. Kimura, Y. Otani, T. Sato, S. Takahashi, S. Maekawa, Phys. Rev. Lett. **98** (2007)
59. N.P. Stern, S. Ghosh, G. Xiang, M. Zhu, N. Samarth, D.D. Awschalom, Phys. Rev. Lett. **97** (2006)
60. T. Sato, K. Nakayama, Y. Sekiba, P. Richard, Y. M. Xu, S. Souma, T. Takahashi, G.F. Chen, J.L. Luo, N.L. Wang, H. Ding, Phys. Rev. Lett. **103** (2009)
61. H. Hiramatsu, S. Matsuda, H. Sato, T. Kamiya, H. Hosono, Acs Appl. Mater. Inter. **6**, 14293 (2014)
62. T. Hatakeyama, H. Sato, H. Hiramatsu, T. Kamiya, H. Hosono, Appl. Phys. Express **9** (2016)
63. A.A. Volykhov, V.I. Shtanov, L.V. Yashina, Inorg. Mater. **44**, 345 (2008)
64. T. Inoue, H. Hiramatsu, H. Hosono, T. Kamiya, Chem. Mater. **28**, 2278 (2016)
65. H. Ohta, Y. Sato, T. Kato, S. Kim, K. Nomura, Y. Ikuhara, H. Hosono, Nature Commun. **1**, 118 (2010)
66. H. Ohta, J. Mater. Sci. **48**, 2797 (2013)
67. T. Katase, Y. Suzuki, H. Ohta, Adv. Electron. Mater. **2** (2016)
68. T. Katase, T. Onozato, M. Hirono, T. Mizuno, H. Ohta, Sci. Rep-UK **6** (2016)

69. H. Taguchi, M. Shimada, M. Koizumi, J. Solid State Chem. **29**, 221 (1979)
70. Y. Takeda, R. Kanno, T. Takada, O. Yamamoto, M. Takano, Y. Bando, Z. Anorg. Allg. Chem. **541**, 259 (1986)
71. C.G. Granqvist, Sol. Energy Mater. Sol. Cells **60**, 201 (2000)